Tailoring Charge and Mass Transport in Cation/Anion-codoped Ni₃N / N-doped CNT Integrated Electrode toward Rapid Oxygen Evolution for Fast-Charging Zinc-Air Batteries

Qian Lu [a], Xiaohong Zou [a], Cuie Wang [b], Kaiming Liao [a, *], Peng Tan [c], Ran Ran [a], Wei Zhou [a], Meng Ni [d], Zongping Shao [a, *]

[a] State Key Laboratory of Materials-Oriented Chemical Engineering,

College of Chemical Engineering, Nanjing Tech University, Nanjing 210009, China

[b] College of Food Science and Light Industry, Nanjing Tech University, Nanjing,

Jiangsu 211816, China

[c] Department of Thermal Science and Energy Engineering,

University of Science and Technology of China, Hefei 230026, Anhui, China

[d] Department of Building and Real Estate, The Hong Kong Polytechnic University,

Hung Hom, Kowloon, Hong Kong 999077, China

Q. Lu and X. Zou contributed equally to this work.

* Corresponding Author,

 E-mail addresses: kaimingliao@njtech.edu.cn; shaozp@njtech.edu.cn

Tailoring Charge and Mass Transport in Cation/Anion-codoped Ni$_3$N / N-doped CNT Integrated Electrode toward Rapid Oxygen Evolution for Fast-Charging Zinc-Air Batteries

Abstract: Searching for the highly active and low cost electrocatalysts with fast-charging capability for rechargeable zinc-air batteries are paramount in terms of their commercial-scale application. Here, we propose an innovative cation/anion-codoped nickel nitrides (FC-Ni$_3$N) along with creating 3D architecture by integrating N-doped carbon nanotubes (NCNT), which is found to be an outstanding bifunctional oxygen electrocatalyst for Zn-air batteries with ultrafast charging rate (Potential =2.02V at 50 mA cm^{-2} with area capacity of 4 mAh cm^{-2}) and long cycling life (700 cycles at 20 mA cm^{-2}). Through varying the cation/anion moiety, the optimal FC-Ni$_3$N/NCNT shows low overpotential of 260 mV at 10 mA cm^{-2} and Tafel slope of 46 mV dec^{-1}, much outperforming the RuO$_2$ benchmark with overpotential of 337 mV and Tafel slope of 91 mV dec^{-1}. The extraordinary oxygen evolution reaction performance (corresponding to the charge process) stems from the simultaneous regulation of charge- and mass-transport kinetics in air electrodes. The proposed strategy and results may pave the way for promoting commercial application of rechargeable zinc-air batteries or other metal-air batteries.

Keywords: Zinc-air battery; Fast charging; Kinetics overpotential; Chemisorption; Nickel nitride catalyst.

Introduction

Rechargeable zinc-air batteries (ZABs) are recognized as one of the most promising power sources because of their high energy density, low cost, ecofriendly, and high safety.[1-4] Recently, rechargeable ZABs are entering the electric vehicle industries dedicated to reducing greenhouse gas emission and fossil fuel consumption.[5-7] Compared to the refueling of petrol vehicles, long charging time of electric vehicles is a real issue hindering their wider applications.[8-10] Fast charging capability has therefore become one of the key features targeted by electric vehicle industries. In response, goals for fast-charging electric vehicle batteries by 2023 is 15 min charging for 80% of the battery capacity (proposed by the US Advanced Battery Consortium).[11] However, rechargeable ZABs suffer the sluggish kinetics of the oxygen evolution reaction (OER, corresponding to the charge processes) that occurs over the air electrode, leading to poor charging rate, large charge overpotential, and short life-span.[12] Therefore, efforts for rechargeable ZABs are urgently needed to achieve the fast-charging goal without negatively affecting electrochemical performances.

To date, various electrocatalysts have been investigated in relation to OER properties, including noble metal oxides (RuO_2, IrO_2) and transition metal compounds.[1, 2, 13] As for noble metal electrocatalysts, low natural abundance and high cost limit their application in industrial scale ZABs.[14] Therefore, much effort has been devoted to explore the noble-metal-free electrocatalysts for practical ZABs, such as transition metal-based oxides (spinel oxides,[15] perovskite oxides[16]), sulfides[17], and nitrides[18, 19]. In particular, transition metal Ni-based oxides[20], phosphides[21], sulfides[21], nitrides[22], hydroxide[23], and layer double hydroxide[24], have been most extensively explored for OER electrocatalysts due to the advantages of earth's abundance, low cost, and adjustable electronic structure.

Nevertheless, the majority of these Ni-based electrocatalysts are either semiconductors or intrinsic insulators, which greatly hinders electron transfer among the electrocatalyst, supporting electrode and reactants,[22] thereby restricting their attempts to build practical rechargeable ZABs with fast-charging capability. Recently, Ni-based metallic nitrides (e.g., Ni_3N),[22, 25-27] have been reported to exhibit improved OER activity compared to their insulating/semiconducting counterparts, which is attributed to the better electron transport inside the bulk electrocatalysts. Interestingly, in our past research of perovskite-based electrocatalyst for OER, obvious improvement of the electron conductivity could be achieved through an anion-doping strategy.[28] Meanwhile, another challenge of Ni-based nitrides is the large kinetics overpotentials over the OER process because of the poor chemisorption of reactant OH^-.[27] Previous studies have demonstrated that cation-doping (e.g., Ni_3FeN, Ni_2Mo_3N)[29, 30] is a promising strategy for tuning the electronic structure of Ni 3d orbit to reduce the adsorption energy of oxygen-related species on Ni-based nitrides. Although progress has been made in Ni-based electrocatalysts, it is still far from meeting the requirements for practical application in fast-charging ZABs.

In addition to internal electron transport in the bulk electrocatalysts, external electron and mass transport in the whole air electrodes has recently been found to also be crucial to their overall performance in rechargeable ZABs, especially for charging at a high rate.[31, 32] As for conventional air electrode, the OER electrocatalyst was loaded on the surface of the ORR electrocatalyst through time-consuming ball milling or vigorous stirring.[16, 30, 33] However, the mixed OER/ORR electrocatalysts are usually not strong enough to endow long-term reversible cycling in ZABs due to the disturbing O_2 bubbles. Once the OER electrocatalyst lose contact with the support of ORR electrocatalyst, sharp increase in kinetics overpotentials will occur. To this end,

the graphene[34], carbon nanotube[35], nanofiber[36], porous carbon[37], and their mixtures[32, 38] were extensively explored as the supports to create OER-ORR bifunctional oxygen electrocatalysts with three-dimensional (3D) framework for promoting electron and mass transport. Among these carbon-based supports, the commercially available carbon nanotubes (CNTs) show obvious superiority from the viewpoint of low cost, light weight, high conductivity and stability.[15, 35, 39] Besides, one-dimensional materials are easily entangled to form porous three-dimensional framework.[32] Moreover, the CNTs could be easily doped by nitrogen to form nitrogen-doped CNTs, guaranteeing good ORR kinetics.[35, 39] Based on above mentioned analysis, optimizing component and structural design by integrating cation/anion-codoped nickel nitrides and NCNTs for achieving both fast electron and mass transfer are imperative for practical rechargeable ZABs with fast charging capability.

Herein, we developed a cation/anion-codoping method to create a noble-metal-free bifunctional electrocatalyst with a 3D cross-linked architecture by combining Fe, Cl-codoped nickel nitride (FC-Ni_3N) nanoparticles and tentacle-liked N-doped CNT (NCNT). The FC-Ni_3N was in situ grown on NCNT and denoted as FC-Ni_3N/NCNT, which is found to be an outstanding OER catalyst with ultralow charge-transfer impedance, fast charging rate, and long cycling life. The extraordinary OER performance stems from (1) the preferable reactant chemisorption and intrinsic bulk conductivity of the FC-Ni_3N, and (2) the fast electron transfer and product dissociation ability in the overall FC-Ni_3N/NCNT electrode with 3D cross-linked architecture, guaranteeing good charge-transfer and mass-transport kinetics. As a result, the FC-Ni_3N/NCNT shows the low overpotential of 260 mV at 10 mA cm^{-2} and low Tafel slope of 46 mV dec^{-1}, much outperforming the RuO_2 benchmark with overpotential of 337

4

mV and Tafel slope of 91 mV dec^{-1}. As expected, the ZABs paired with FC-Ni$_3$N/NCNT electrodes show superior durability for over 700 cycles with constant charge potential of 1.96 V at 20 mA cm^{-2}, while the RuO$_2$-based ZAB could only operate for 80 cycles. Specifically, at an ultrahigh charging rate of 50 mA cm^{-2} with a high area capacity of 4 mAh cm^{-2}, rechargeable ZAB with FC-Ni$_3$N/NCNT still displays low charge potential of 2.02 V, surpassing the state-of-the-art RuO$_2$ benchmark of 2.75 V. The fundamental understanding of the charge and mass transport in whole air electrode and the outstanding electrochemical performances are further exploited in details.

Results and discussion

The concept of charge- and mass-transport regulation is illustrated in **Figure 1a**. As for the single Ni$_3$N or FC-Ni$_3$N electrocatalysts (**Figure 1a**, left), sluggish mass transport and slow internal (bulk) or external (electrode) electron transfer are observed during the OER process. It is widely accepted that the OER performance was dependent on three combined processes, including OH$^-$ adsorption (**step 1**), surface reaction (**step 2**, i.e., oxidization of OH$^-$ to O$_2$), and O$_2$ desorption (**step 3** or/and **4**).[40] Although co-doping cation Fe^{3+} and anion Cl$^-$ into Ni$_3$N electrocatalyst could facilitate preferable chemisorption of OH$^-$ and improve the intrinsic bulk conductivity of the FC-Ni$_3$N, the mass transport of O$_2$ and the external electron transfer in whole electrode are still insufficient, especially at a high charging rate. Usually, the OER performance in the fast-charging ZAB was also affected by O$_2$ desorption because the rapidly generated O$_2$ bubbles are easily adhere to the charging electrode, forming a layer of gas membrane around the electrode, resulting in high ohmic resistance, low charging efficiency, and even sudden death of the battery. Fortunately, the 3D tentacle-liked NCNT framework (ORR catalyst) that closely adhered to the FC-Ni$_3$N not only can serve as a conductive

5

network to reduce the OER charge-transfer impedance but also promote rapid transporting of the produced O_2 into the electrolyte (**Figure 1a**, right), allowing the rapid OER kinetics. Thus, the adsorption of reactants, the desorption of product, and the activity of active sites are improved in the new-established FC-Ni_3N/NCNT integrated electrode, guaranteeing rapid electron transfer and fast mass transport in fast-charging ZABs.

Considering above design strategy, the FC-Ni_3N/NCNT and other control catalysts are prepared via the methanol-thermal process and nitridation process (details shown in supporting information). First, a series of Ni-based layered double hydroxides (LDH) /CNT-A are prepared, and the X-ray diffraction pattern (XRD) confirmed that the as-prepared samples are both the crystal structure of LDH (**Figure S1a**). Then, the FC-Ni_3N/NCNT catalyst is obtained after nitridation process and the scanning electron microscopy (SEM) image is shown in **Figure S2a**. The tentacle-liked carbon nanotubes are intertwined with each other to form a three-dimensional conductive matrix, and the FC-Ni_3N nanoparticle are decorated on the surface of NCNT matrix. For comparison, the pure FC-Ni_3N nanoparticle with size lower than 100 nm and FC-NiO/CNT with nanosheet-liked FC-NiO are also presented in **Figure S2b** and **Figure S2c**, respectively. In addition, the FC-Ni_3N/NCNT-X (X = 0.01, 0.02, and 0.04) with different content of $FeCl_2$ are also prepared to explore the optimal doping amount. As shown in **Figure S3**, the particle size of FC-Ni_3N-X increase with the amount of $FeCl_2$. For comparison, as shown in **Figure S4**, the selected control catalysts, such as the Ni_3N/NCNT (without doping Fe and Cl), Cl-Ni_3N/NCNT (without doping Fe), and Ni_3FeN/NCNT (without doping Cl), show the similar microstructures with FC-Ni_3N/NCNT (with doping Fe and Cl).

The morphology of the FC-Ni$_3$N/NCNT is further examined by transmission electron microscopy (TEM). As shown in **Figure 1b** and **Figure S5a**, the intertwined NCNT matrix is decorated by FC-Ni$_3$N nanoparticles with average particle size of 26 nm without obvious agglomeration. In addition, the FC-Ni$_3$N nanoparticles is tightly anchored on the surface of NCNT to form the heterointerface, thus improving the electron and oxygen transport between FC-Ni$_3$N and conductive NCNT matrix as illustration in **Figure 1a** (**Figure 1c**). The detail insight about FC-Ni$_3$N is further explored by high-resolution transmission electron microscopy (HRTEM) in **Figure 1d** and **Figure S5b**. The [1$\bar{1}$0] view direction clearly exhibits the (111), ($\bar{1}\bar{1}$1), and (002) planes, revealing the hexagonal structure of FC-Ni$_3$N,[41-43] and the corresponding fast Fourier transform (FFT) pattern is also indexed to the hexagonal structure with the zone axis of [1$\bar{1}$0] (**Figure 1e**). More importantly, the atomic structure model of the observed [1$\bar{1}$0] zone axis is also presented in the **Figure 1f**, which is well accorded with the actual observation of HRTEM in **Figure 1d**. In addition, the high-angle annular dark field scanning TEM (HAADF-STEM) image and corresponding EDX elemental mapping in **Figure 1g** reveals a uniform distribution of Fe, Ni, N, O and Cl elements for the as-prepared FC-Ni$_3$N nanoparticle and C elements for the NCNT matrix. In general, the O elements is mainly attributed to the surface adsorbed oxygen species. The element content of FC-Ni$_3$N in FC-Ni$_3$N/NCNT is listed in the Table S1, and the atomic ratio Fe and Cl are respectively 11.57% and 0.75%, proving the successful doped of Fe and Cl elements into Ni and N sites in the Ni$_3$N, respectively. Moreover, the mass ratio of FC-Ni$_3$N and NCNT is explored by thermogravimetric analysis (TGA). As shown in **Figure S6**, the mass ratio of FC-Ni$_3$N nanoparticle is about 62.8% in the composite of FC-Ni$_3$N/NCNT.

To further explore the crystalline and electronic structure, X-ray diffraction (XRD), X-ray photoelectron spectroscopy (XPS), and Raman spectroscopy of these as-prepared catalysts are conducted. As shown in **Figure 2a**, both the FC-Ni_3N/NCNT, C-Ni_3N/NCNT and Ni_3N/NCNT reveals the hexagonal crystal structure (JCPDS 01-089-5144), and the two main diffraction peaks of FC-Ni_3N/NCNT at 41.8° and 44.4° are respectively index to (002) and (111),[41, 42] which is also consistent with the observation of HRTEM. More importantly, the position of (111) diffraction peaks follow the sequence of Ni_3N/NCNT > C-Ni_3N/NCNT > FC-Ni_3N/NCNT, which is attributed to the larger ionic diameter of doped Fe and Cl than Ni and N, respectively. As shown in **Figure S1b**, the (111) diffraction angles of FC-Ni_3N-X decrease with increasing the amount of $FeCl_2$. The results of XRD well prove that the Fe and Cl is successfully doped into the lattice of Ni_3N. Moreover, the XPS survey spectra also confirm that the Cl is successfully doped into Ni_3N and the LDHs/CNT is successfully converted to the nitrides/NCNT (**Figure S7**). In addition, the Fe doped Ni_3N/NCNT is also prepared by same procedure. As shown in **Figure S1c**, after replacing the $FeCl_2$ to Fe$(NO_3)_3$, the cubic structure of Ni_3FeN/NCNT is obtained. The transformation of crystal structure is mainly due to the large diameter of Cl than the N element, thus benefitting the substitution of Fe for Ni in the hexagonal Ni_3N.

The insights about the electronic structure of the Ni_3N/NCNT before and after Fe/Cl doping are further explored. As shown in **Figure 2b**, the high-resolution Ni $2p_{3/2}$ spectrum of both the FC-Ni_3N/NCNT, C-Ni_3N/NCNT and Ni_3N/NCNT could be deconvoluted into two peaks attributed to Ni^+ and Ni^{2+}, and other three corresponding satellite peaks.[41, 42, 44] In general, the principal valence state of Ni_3N is monovalent Ni^+, and the existence of Ni^{2+} is mainly caused by the surface oxidation of Ni^+.[41, 42, 44] Similarly, the two Ni^{2+} peaks and two corresponding satellite peaks are also

8

observed for FC-NiO/CNT (**Figure S9a**). To study the doped effect of Cl, XPS peaks of the monovalent Ni^+ is negatively shifted about 0.3 eV for both the FC-Ni$_3$N/NCNT and C-Ni$_3$N/NCNT, revealing the electron-rich Cl could improve the density of free electron around the monovalent Ni^+, thus facilitating the electronic conductivity of bulk FC-Ni$_3$N particle. Therefore, the anion Cl-doped is an available strategy to optimize the electronic conductivity of bulk nitride. In addition, after cation Fe-doped, the XPS peaks of bivalent Ni^{2+} is positively shifted about 0.2 eV for FC-Ni$_3$N/NCNT, revealing the Fe-doped could promote the valence state of surface oxidized Ni^{2+}.[45] Furthermore, the high-resolution Fe 2p spectrum of FC-Ni$_3$N/NCNT is explored. As shown in **Figure 2c** and S8, two Ni Auger peaks located at 705.5 and 712.5 eV are appeared for both Ni-based samples. Except the two Ni Auger peaks, the high-resolution XPS Fe 2p spectrum of FC-Ni$_3$N/NCNT could be deconvoluted into one doublet of Fe^{3+} located at 711.6 eV and 725.2 eV, and one corresponding satellite peak.[39] Similar high-resolution Fe 2p spectrum of FC-NiO/CNT is also exhibited in **Figure S9b**, revealing the surface Fe element in FC-Ni$_3$N/NCNT is easily oxidized to stable valence state of Fe^{3+}. The substitution of partial surface Ni^{2+} to Fe^{3+} could appropriately improve the valence of Ni^{2+} in FC-Ni$_3$N/NCNT, which is beneficial for enhancing the adsorption energy toward oxygen species during the OER process.[46] In addition, the relative ratio of surface Ni^{2+} and Ni^+ is also affected by cation Fe-doping. As previously reported, the high oxidation state of bivalent Ni^{2+} is the main active site for OER. As shown in **Figure 2d**, the area ratio of surface Ni^{2+} is up to 91.0% for the FC-Ni$_3$N/NCNT, which is obviously larger than that of C-Ni$_3$N/NCNT with 84.1% and Ni$_3$N/NCNT with 83.3%. Therefore, the high content of Ni^{2+} in the surface of FC-Ni$_3$N/NCNT is beneficial for the OER compared with C-Ni$_3$N/NCNT and Ni$_3$N/NCNT. The high-resolution N 1s spectrum also exhibits the peaks located at 400 eV, which is mainly attributed to the

nitrogen-doped into carbon skeleton (**Figure 2e**).[47] Fortunately, the nitrogen atom in the CNT could regulate the adjacent carbon atoms, further optimizing the adsorption of oxygen and breaking the O-O bond, which is extremely beneficial to ORR process.[47] Moreover, the nitrogen in CNT could also facilitate the adsorption of oxygen overflowing from the surface of nitride during OER process especially at high current, thus providing a possible path for desorption of oxygen from catalysts surface. In addition, the positive shift of XPS N-Fe/Ni peak also proves the successful substitution of Ni to Fe in the FC-Ni_3N.[48] The Raman spectroscopy is further applied to analyze the phase composition of these catalysts. As shown in **Figure 2f**, the Raman shift at 554 cm^{-1} for FC-Ni_3N/NCNT can be attributed to one-phonon (1P) Ni–O modes (LO).[49] Compared to Ni_3N/NCNT, the shift of 1P LO mode for FC-Ni_3N/NCNT suggests that Fe is successfully doped into the lattice of Ni-O.[49] The same Raman shift of 1P LO mode for FC-Ni_3N/NCNT, FC-NiO/NCNT and FC-Ni_3N reveals that the formation of Ni-O bond is mainly attributed to the surface oxidation of Ni^+ to Ni^{2+}, which is well consistent with the results of XPS Ni $2p_{3/2}$ in **Figure 2b** (**Figure S10**). In addition, compared to NCNT, the positive shift of defective carbon atoms (D band) and negative shift of sp^2-graphitic carbon (G band) are observed for nitrides/NCNT composites, revealing the existence of electronic interaction between nitrides and NCNT,[50] which is also consistent with the observation of interface between nitrides and NCNT in **Figure 1b**. From the results of XRD, XPS and Raman spectroscopy, the crystal structure of FC-Ni_3N/NCNT is finally constructed in **Figure 2g**. In detail, the Ni and N are respectively replaced by the Fe and Cl in the lattice of Ni_3N and the FC-Ni_3N is tightly anchored on the surface of NCNT by the nitrogen site to construct the FC-Ni_3N/NCNT composite.

To evaluate the oxygen evolution electrocatalytic activity, the linear sweep voltammetry (LSV) is conducted in the O_2-saturated 0.1 M KOH electrolyte at rotating speeds of 1600 rpm. Firstly, the optimal doping contents of Fe and Cl is considered in **Figure S11**, revealing that the FC-Ni$_3$N/NCNT-0.03 (0.03 means the gram of FeCl$_2$·4H$_2$O, simplify to FC-Ni$_3$N/NCNT) shows best OER performance than other control samples. Secondly, the comparison of OER performance between nitride/NCNT and counterpart oxide/NCNT are exhibited in **Figure S12**, proving that the performance of nitride/NCNT is obviously better than oxide/NCNT. The active site for nitride and oxide both are the bivalent Ni^{2+}, therefore, the better OER performance of nitride is mainly attributed to its superior bulk electrical conductivity compared to oxide (**Figure 1a**).[22] Finally, the comparison between FC-Ni$_3$N/NCNT and FC-Ni$_3$N are also conducted to explore the effect of NCNT matrix. As shown in **Figure S13a**, the improved ORR performance is mainly attributed to the NCNT matrix for the FC-Ni$_3$N/NCNT. In addition, the OER performance of FC-Ni$_3$N is significantly improved after combining with NCNT matrix (**Figure S13**), revealing the building of conductive matrix could facilitate the electron and oxygen transport through the whole electrode (**Figure S13d**), thus improving the apparent OER activity. Therefore, the integration of nitride and NCNT matrix towards the electron conductivity is the best choice to construct superior OER catalyst for fast charging ZABs.

The effect of Fe and Cl doping toward OER is further explored for the optimal FC-Ni$_3$N/NCNT, and the commercial RuO_2 benchmark is also examined for comparison. As shown in **Figure 3a**, the FC-Ni$_3$N/NCNT obviously exhibits higher catalytic current and lower onset potential than other contrastive Ni$_3$FeN/NCNT, C-Ni$_3$N/NCNT, Ni$_3$N/NCNT, and even benchmark RuO_2 catalysts. In general, the overpotential (η) at current density of 10 mA cm^{-2} is a critical criterion to assess the OER activity.[14, 47]

Significantly, the FC-Ni$_3$N/NCNT achieve an ultra-low overpotential of 260 mV at 10 mA cm^{-2}, while Ni$_3$N/NCNT, Ni$_3$FeN/NCNT, C-Ni$_3$N/NCNT and RuO$_2$ exhibits overpotential of 370, 270, 352 and 337 mV, respectively. More importantly, the mass activity (MA, current per mass of catalysts) and specific activity (SA, current per specific surface area) are the critical criterion for practical applications and intrinsic activity of these catalysts, respectively.[51] The Brunauer–Emmett–Teller (BET) surface areas of FC-Ni$_3$N/NCNT, Ni$_3$N/NCNT, Ni$_3$FeN/NCNT and C-Ni$_3$N/NCNT are 124, 135, 166 and 123 m^2 g^{-1}, respectively (**Figure S14**). As shown in **Figure 3b**, the FC-Ni$_3$N/NCNT provides a MA of 241.6 A g$^{-1}_{cat}$ and SA of 0.097 mA cm$^{-2}_{BET}$ at η = 300 mV, which are 23.70, 2.36, and 35.90 times of MA and 25.79, 3.16, 35.93 times of SA higher than Ni$_3$N/NCNT, Ni$_3$FeN/NCNT and C-Ni$_3$N/NCNT, respectively. Moreover, the MA of FC-Ni$_3$N/NCNT is 10.72 times higher than that of the benchmark RuO$_2$, implying the superior OER performance for the designed FC-Ni$_3$N/NCNT. To further examine the kinetics of OER, Tafel plots of as-prepared catalysts is obtained in **Figure 3c**. In general, the low Tafel slope reveals the rapid OER kinetics.[30] The Tafel plots of FC-Ni$_3$N/NCNT (46 mV dec^{-1}) is obviously lower than that of the Ni$_3$N/NCNT (107 mV dec^{-1}), Ni$_3$FeN/NCNT (73 mV dec^{-1}), C-Ni$_3$N/NCNT (61 mV dec^{-1}) and RuO$_2$ (91 mV dec^{-1}), indicating the faster OER kinetics for the Fe and Cl codoped Ni$_3$N/NCNT than other control catalysts. Surprisingly, the OER catalytic activity of our work is also comparable to that of recently reported transition metal-based catalyst (**Figure 3d** and **Table S3**). Moreover, the charge transfer impedance is also applied to assess the OER performance. As shown in **Figure 3e** and **Figure S15** for the EIS Nyquist plots, the charge transfer impedance of FC-Ni$_3$N/NCNT is just 11.6 Ω, which is obviously lower than that of the Ni$_3$N/NCNT (99.3 Ω), Ni$_3$FeN/NCNT (15.4 Ω), C-Ni$_3$N/NCNT (32.8 Ω), and even the benchmark RuO$_2$ (67.2 Ω). The long-term stability

is another critical indicator to evaluate the practical application of designed catalyst. In **Figure 3f**, the overpotential for FC-Ni$_3$N/NCNT just increase about 13 mV after 12 h chronopotentiometry measurement, while the benchmark RuO$_2$ increase 216 mV after 5 h test, showing the excellent electrochemical stability for the designed FC-Ni$_3$N/NCNT.

In order to assess the performance of ZAB, the ORR performances of the as-prepared catalysts are further explored in **Figure S16a**. The limiting diffusion current of nitrides/NCNT is obviously higher than NCNT and oxides/CNT, revealing the high reaction kinetics current for the configuration of nitrides/NCNT. The potential of these catalysts at constant current density of -2 mA cm^{-2} are exhibited in the **Figure S16b**, further confirming the FC-Ni$_3$N/NCNT owns excellent ORR performance compared to other control catalysts. In addition, the chronoamperometric response of ORR at 0.30 V (vs. RHE/V) for FC-Ni$_3$N/NCNT and benchmark Pt/C are also adopted to evaluate the long-term durability. In **Figure S16c**, the FC-Ni$_3$N/NCNT exhibits the current decay rate of 14.35% after 10 h, which is obviously better than that of the benchmark Pt/C (25.62%). Therefore, except for the superior OER performance, the FC-Ni$_3$N/NCNT also exhibits excellent ORR performance. The bifunctionality performance of the FC-Ni$_3$N/NCNT is finally examined by potential gap (ΔE) between the potential at 10 mA cm^{-2} for OER and the half-wave potential for ORR. As shown in **Figure 4a**, the potential gap of FC-Ni$_3$N/NCNT is just 0.79 V, which even approach to the benchmark mixture of Pt/C and RuO$_2$ with 0.85 V.

The practical application of the optimal FC-Ni$_3$N/NCNT in ZABs is further explored. For comparison, the mixture of benchmark Pt/C and RuO$_2$ (Pt/C + RuO$_2$) is also used to construct the air electrode. As shown in **Figure 4b**, the ZABs is fabricated by air electrode with FC-Ni$_3$N/NCNT or benchmark Pt/C + RuO$_2$ (with the loading

13

amount of 1 mg cm^{-2}), aqueous electrolyte with 6.0 M KOH + 0.2 M ZnCl$_2$, and anode with high purity zinc plate. In addition, the fabrication process of an air electrode for Zn-air batteries was presented in **Figure S17**. **Figure 4c** exhibits the charge/discharge polarization curves of the ZABs with the FC-Ni$_3$N/NCNT and Pt/C + RuO$_2$ as the air electrode. The discharge potentials of FC-Ni$_3$N/NCNT is slightly lower than the Pt/C + RuO$_2$, which is consistent with the results of ORR (**Figure 4a**). In addition, the power density of FC-Ni$_3$N/NCNT is 139.5 mW cm^{-2}, while that of the Pt/C + RuO$_2$ is 157.4 mW cm^{-2} (**Figure S18a**). Notably, the FC-Ni$_3$N/NCNT based air electrode exhibits ultra-low charge overpotential of 0.37 and 0.48 V to respectively deliver the current density of 50 and 100 mA cm^{-2}, which are significantly lower than the Pt/C + RuO$_2$ based air electrode from the charging polarization curves (**Figure 4c**), agreeing well with the above OER results.

Then, the charging rate performance of FC-Ni$_3$N/NCNT and benchmark catalysts Pt/C (ORR) and RuO$_2$ (OER) are further evaluated by galvanostatic charge/discharge test. As shown in **Figure 4d** and **S18b**, the FC-Ni$_3$N/NCNT based ZABs could achieve the charge potential of 1.94, 1.96, 1.98, 2.00, and 2.02 V at 10, 20, 30, 40, and 50 mA cm^{-2}, respectively, while that of 2.04, 2.13, 2.25, 2.39, and 2.75 V for Pt/C + RuO$_2$, strongly proving the superior charging rate performance for the designed catalysts. Not only that, the charge potential could retain the initial condition after the current density recovering to initial condition, and this rating test process could steadily recycle for 4 times (about 120 h) without any deterioration of the charge/discharge potential. For comparison, the charge potential is sharply increased after the current density recovering to initial condition for Pt/C + RuO$_2$. In addition, the voltage-area capacity curves are presented in **Figure 4e** and **S18c**. The round-trip efficiencies of FC-Ni$_3$N/NCNT are 60.8%, 60.3%, 59.7%, 59.3%, and 58.6% when charging respectively

at 10, 20, 30, 40, and 50 mA cm^{-2} along with constantly discharge at 5 mA cm^{-2}. In contrast, the round-trip efficiencies are just 60.1%, 56.8%, 53.7%, 50.5%, and 41.3% for Pt/C + RuO$_2$ catalyst. Specially, FC-Ni$_3$N/NCNT based air electrode achieve the target of fast charging ZABs with discharge for 50 min at 5 mA cm^{-2} and charge for just 5 min at 50 mA cm^{-2} under the area capacity of 4 mAh cm^{-2} with high round-trip efficiency of 58.6%. Then, the cycling performance of rechargeable ZABs is further evaluated by the galvanostatic charge/discharge test to assess the durability of designed catalyst. When cycling at 10 mA cm^{-2} (**Figure S18d**), the ZABs with FC-Ni$_3$N/NCNT shows ultra-stable cycling performance for 200 h with the initial polarization potential of 0.77 V (charge potential of 1.94 V) and last polarization potential of 0.80 V (charge potential of 1.93 V). The result further confirms the superior electrochemical stability of the designed FC-Ni$_3$N/NCNT. The rate performance is also considered by the galvanostatic charge/discharge test at 20 mA cm^{-2} with the area capacity of 1.65 mAh cm^{-2}. In **Figure 4f**, the initial charge/discharge polarization potential is just 0.90 V for FC-Ni$_3$N/NCNT based ZABs with the charge potential of 1.96 V. After operating for 700 cycles, the polarization potential is slightly reduced to 0.88 V with the constant charge potential of 1.96 V. For comparison, the Pt/C + RuO$_2$ based ZABs could just operate for 80 cycles with the finally polarization potential of 1.29 V (charge potential of 2.18 V). The high-rate charging performance is mainly attributed to the rational design of Fe and Cl co-doped Ni$_3$N loaded intertwined NCNT matrix with excellent catalytic activity and conductivity, and much faster than previous reported ZABs with transition metal-based catalysts (**Table S4**).

In order to probe the structural stability and active site, the cyclic voltammetry for 1000 cycles is adopted in **Figure 5a** and **Figure S19**, revealing the ultra-stable OER performance for the nitride-based catalysts. The redox couple of Ni^{2+} and Ni^{3+} is

obviously observed for both the FC-Ni$_3$N/NCNT and Ni$_3$N/NCNT, which have been detail explored in most of Ni-based electrocatalysts.[22, 33, 52] In addition, the initial hexagonal crystal structure is remained without any impure materials for the XRD patterns of FC-Ni$_3$N/NCNT after 1000 CV test (**Figure 5b**), further revealing the excellent structural stability of the designed FC-Ni$_3$N/NCNT catalyst. Moreover, the SEM and TEM image of FC-Ni$_3$N/NCNT after 1000 CV test also proves that the microstructure of FC-Ni$_3$N anchored NCNT matrix is well maintained (**Figure 5c** and **S20a**). Therefore, these results strongly confirm the superior electrochemical stability of the designed FC-Ni$_3$N/NCNT towards OER process. More importantly, an amorphous layer is covered on the surface of bulk FC-Ni$_3$N after CV test for the FC-Ni$_3$N/NCNT from HRTEM image (**Figure 5d**). After CV test, the hexagonal crystal structure of bulk FC-Ni$_3$N is well reserved from the crystal lattice and corresponding FFT pattern (inset in **Figure 5d**). Therefore, the actual OER active site of FC-Ni$_3$N/NCNT is the surface amorphous layer, and the similar results is easily observed from previous reported nitride-based catalyst.[30] In addition, the high-angle annular dark field scanning TEM (HAADF-STEM) image and corresponding EDX elemental mapping in **Figure 5e** reveals a uniform distribution of Fe, Ni, N, O and Cl elements for the FC-Ni$_3$N/NCNT after CV test, and the element content of FC-Ni$_3$N after CV test in FC-Ni$_3$N/NCNT is listed in the Table S2. The contents of Cl with atomic ratio of 0.61% and Fe with atomic ratio of 9.65% is slightly reduced after 1000 CV test, revealing the element composition of the bulk FC-Ni$_3$N nanoparticle is perfectly remained and the surface element composition is inevitably changed.

The surface amorphous layer is further explored by the XPS spectra in detail. In **Figure 6a**, the doublets of Cl 2p is disappeared after OER test for the FC-Ni$_3$N/NCNT, revealing the Cl could leach out during the OER process. Therefore, the surface oxygen

vacancy may be formed by the Cl leaching, thus benefiting the adsorption of oxygen species.[15, 53] In addition, for the XPS peak of Ni^{2+}, the positive shift of 0.3 eV is also observed for FC-Ni_3N/NCNT compared with Ni_3N/NCNT after 1000 CV test (**Figure 6b**), and the Fe 2p spectrum of FC-Ni_3N/NCNT after 1000 CV test could be deconvoluted into one doublet of Fe^{3+} located at 711.6 and 725.2 eV (**Figure 6c**). Therefore, the positive shift of Ni^{2+} is ascribed to the doping of Fe^{3+} in the surface layer. Moreover, the XPS peaks of Ni^+ and N-Fe/Ni are both disappeared from the Ni $2p_{3/2}$ (**Figure 6b**) and N 1s (**Figure S20b**) spectrums, which further proves the surface reconstruction of FC-Ni_3N/NCNT after OER test, similarly to previous reported nitride-based catalysts. Finally, the high-resolution O 1s spectrum of FC-Ni_3N/NCNT and Ni_3N/NCNT after CV test are exhibited in **Figure 6d**. In general, the mechanism of Ni-based catalysts in alkaline electrolyte [22] could be concluded as follow:

$$Ni^{2+} + 3OH^- \rightarrow NiOOH + H_2O + e^- \qquad (1)$$

$$NiOOH + OH^- \rightarrow NiO(OH)_2 + e^- \qquad (2)$$

$$NiO(OH)_2 + 2OH^- \rightarrow NiOO_2 + 2H_2O + 2e^- \qquad (3)$$

$$NiOO_2 + OH^- \rightarrow NiOOH + O_2 + e^- \qquad (4)$$

Summary reaction: $4OH^- \rightarrow O_2 + 2H_2O + 4e^-$

As above overall reactions, the high-resolution XPS O 1s spectrum of FC-Ni_3N/NCNT and Ni_3N/NCNT after CV test could be deconvoluted into three peaks attributed to the OER-involved oxygen-related species of OH^-, O_2* and H_2O*. Specially, the binding energy of OH^- for FC-Ni_3N/NCNT positively shift about 1.0 eV compared with Ni_3N/NCNT after CV test. The surface reaction for OER process is tightly related to the adsorption of OH^- from the electrolyte.[14, 39] Therefore, the high binding energy of Fe/Ni-based active site towards OH^- could efficiently improve the adsorption energy of OH^*-related intermediate species, thus facilitating the surface

17

reaction kinetics and further enhancing the OER performance.[39] In addition, the binding energy of FC-Ni$_3$N/NCNT after CV test is slightly increased about 0.3 eV for both the O$_2$* and H$_2$O* compared with Ni$_3$N/NCNT. As a result, desorption of O$_2$* form the surface of FC-Ni$_3$N is slightly impeded in some degree. Owning to the nitrogen site in NCNT could bind with O$_2$*, the generated O$_2$* on surface of FC-Ni$_3$N could overflow to the surface NCNT, thus facilitating desorption of O$_2$* during OER process.[16, 54] Furthermore, the density of states (DOS) of FC-Ni$_3$N and Ni$_3$N by the density functional theory (DFT) calculations were shown in **Figure 6e**. In detail, near Fermi level, the DOS of FC-Ni$_3$N is more intense than that of Ni$_3$N, suggesting that the carrier concentration and electrical conductivity after Fe,Cl co-doping were improved, which is consistent with the results of XPS (**Figure 2b**). Considering above analysis, the reaction mechanism of OER is concluded in **Figure 6f**. The Fe doped Ni-based amorphous oxide layer on the surface of FC-Ni$_3$N is the actual OER active site, and the strategy of Fe, Cl-doping could improve the bulk electron conductivity, thus enhancing the bulk transport of generated electron on the surface oxide layer. In addition, the tight couple of FC-Ni$_3$N nanoparticle and NCNT matrix could also improve the transport of electron through the whole catalyst layer. Moreover, the generated abundant oxygen anchored on surface of nitride, which may isolate the contact between nitride and electrolyte, could overflow to the surface of NCNT anchored by the nitrogen site. The moderate binding energy of NCNT towards oxygen species could facilitate the oxygen desorption especially when ZABs charge at a high rate.

Conclusions

In summary, a noble-metal-free Ni-based bifunctional electrocatalyst with a 3D cross-linked nanoweb architecture was successfully synthesized via a facile two-step process. The co-doping Fe^{3+} and Cl$^-$ into Ni$_3$N takes advantages of improved bulk

conductivity and preferable chemisorption of OH$^-$, while the tentacle-liked N-doped CNT endows rapid O$_2$ bubble's desorption and the electron transfer in whole electrode, resulting in synergistic improvement in fast-charging Zn-air batteries. As expected, the optimal FC-Ni$_3$N/NCNT achieves enhanced OER catalytic activity compared with FC-Ni$_3$N, Ni$_3$FeN/NCNT, C-Ni$_3$N/NCNT and Ni$_3$N/NCNT, with ultra-low overpotential of 260 mV at 10 mA cm^{-2} and Tafel slope of 46 mV dec^{-1}. In addition, the NCNT matrix could also enhance the ORR performance of FC-Ni$_3$N with half-wave potential of 0.70 V. Therefore, the ZABs with FC-Ni$_3$N/NCNT based air electrode shows excellent charge rate performance up to 50 mA cm^{-2} with the charge potential of 2.02 V (area capacity of 4 mAh cm^{-2}) and round-trip efficiency of 58.6% (discharge at 5 mA cm^{-2}). Particularly, the ZABs could operate at high current density of 20 mA cm^{-2} (area capacity of 1.65 mAh cm^{-2}) for 700 cycles with ultra-low charge potential of 1.96 V, which is obviously better than the state-of-the-art catalyst benchmark (Pt/C + RuO$_2$) with the charge potential of 2.18 V after 80 cycles. This work presents a synergistic way to design the efficient bifunctional electrocatalyst for fast-charging rechargeable ZABs, revealing new protocol for the future design of other metal-air battery systems.

Appendix A. Supplementary material

Supplementary data associated with this article can be found in the online version at XXX.

Declarations of interest:

The authors declare no competing financial interest.

Acknowledgements

Reference:
[1] Y. Zhang, B. Chen, D. Guan, M. Xu, R. Ran, M. Ni, W. Zhou, R. O'Hayre, Z. Shao, Nature, 591 (2021) 246-251.

[2] C. Niu, J. Liu, T. Qian, X. Shen, J. Zhou, C. Yan, Natl. Sci. Rev., 7 (2020) 315-323.

[3] Y. Zhong, X. Xu, W. Wang, Z. Shao, Batteries Supercaps, 2 (2018) 272-289.

[4] J. Yi, P. Liang, X. Liu, K. Wu, Y. Liu, Y. Wang, Y. Xia, J. Zhang, Energy Environ. Sci., 11 (2018) 3075-3095.

[5] K. Liao, S. Wu, X. Mu, Q. Lu, M. Han, P. He, Z. Shao, H. Zhou, Adv. Mater., 30 (2018) 1705711.

[6] X. Zou, K. Liao, D. Wang, Q. Lu, C. Zhou, P. He, R. Ran, W. Zhou, W. Jin, Z. Shao, Energy Storage Mater., 27 (2020) 297-306.

[7] X. Zou, Q. Lu, Y. Zhong, K. Liao, W. Zhou, Z. Shao, Small, 14 (2018) 1801798.

[8] G.-L. Zhu, C.-Z. Zhao, J.-Q. Huang, C. He, J. Zhang, S. Chen, L. Xu, H. Yuan, Q. Zhang, Small, 15 (2019) 1805389.

[9] S. Liu, M. Wang, H. Ji, X. Shen, C. Yan, T. Qian, Natl. Sci. Rev., 2020, DOI: 10.1093/nsr/nwaa136.

[10] Q. Lu, X. Zou, R. Ran, W. Zhou, K. Liao, Z. Shao, J. Mater. Chem. A, 7 (2019) 22463-22474.

[11] Y. Liu, Y. Zhu, Y. Cui, Nat. Energy, 4 (2019) 540-550.

[12] Y. Zhong, X. Xu, P. Liu, R. Ran, S.P. Jiang, H. Wu, Z. Shao, Adv. Energy Mater., 10 (2020) 2002992.

[13] S. Ren, X. Duan, S. Liang, M. Zhang, H. Zheng, J. Mater. Chem. A, 8 (2020) 6144-6182.

[14] Q. Lu, Y. Guo, P. Mao, K. Liao, X. Zou, J. Dai, P. Tan, R. Ran, W. Zhou, M. Ni, Z. Shao, Energy Storage Mater., 32 (2020) 20-29.

[15] X.T. Wang, T. Ouyang, L. Wang, J.H. Zhong, Z.Q. Liu, Angew. Chem., Int. Ed., 59 (2020) 6492-6499.

[16] X. Wang, J. Sunarso, Q. Lu, Z. Zhou, J. Dai, D. Guan, W. Zhou, Z. Shao, Adv. Energy Mater., 10 (2019) 1903271.

[17] W. Liu, J. Zhang, Z. Bai, G. Jiang, M. Li, K. Feng, L. Yang, Y. Ding, T. Yu, Z. Chen, A. Yu, Adv. Funct. Mater., 28 (2018) 1706675.

[18] C. Zhu, Z. Yin, W. Lai, Y. Sun, L. Liu, X. Zhang, Y. Chen, S.-L. Chou, Adv. Energy Mater., 8 (2018) 1802327.

[19] Y.P. Deng, Y. Jiang, R. Liang, S.J. Zhang, D. Luo, Y. Hu, X. Wang, J.T. Li, A. Yu, Z. Chen, Nat. Commun., 11 (2020) 1952.

[20] C. Kuai, Y. Zhang, L.-L. Han, H.L. Xin, C. Sun, D. Nordlund, S. Qiao, X.-W. Du, F. Lin, J. Mater. Chem. A, 8 (2020) 10747-10754.

[21] X. Wang, W. Li, D. Xiong, D.Y. Petrovykh, L. Liu, Adv. Funct. Mater., 26 (2016) 4067-4077.

[22] K. Xu, P. Chen, X. Li, Y. Tong, H. Ding, X. Wu, W. Chu, Z. Peng, C. Wu, Y. Xie, J. Am. Chem. Soc., 137 (2015) 4119-4125.

[23] D. Zhu, J. Liu, L. Wang, Y. Du, Y. Zheng, K. Davey, S.-Z. Qiao, Nanoscale, 11 (2019) 3599-3605.

[24] L. Yu, J.F. Yang, B.Y. Guan, Y. Lu, X.W. Lou, Angew. Chem., Int. Ed., 57 (2018) 172-176.

[25] A. Wu, Y. Xie, H. Ma, C. Tian, Y. Gu, H. Yan, X. Zhang, G. Yang, H. Fu, Nano Energy, 44 (2018) 353-363.

[26] T. Liu, M. Li, C. Jiao, M. Hassan, X. Bo, M. Zhou, H.-L. Wang, J. Mater. Chem. A, 5 (2017) 9377-9390.

[27] X. Gao, X. Liu, W. Zang, H. Dong, Y. Pang, Z. Kou, P. Wang, Z. Pan, S. Wei, S. Mu, J. Wang, Nano Energy, 78 (2020) 105355.

[28] Y. Zhu, Q. Lin, Z. Wang, D. Qi, Y. Yin, Y. Liu, X. Zhang, Z. Shao, H. Wang, J. Energy Chem., 52 (2021) 115-120.

[29] X. Jia, Y. Zhao, G. Chen, L. Shang, R. Shi, X. Kang, G.I.N. Waterhouse, L.-Z. Wu, C.-H. Tung, T. Zhang, Adv. Energy Mater., 6 (2016) 1502585.

[30] Y. Yuan, S. Adimi, X. Guo, T. Thomas, Y. Zhu, H. Guo, G.S. Priyanga, P. Yoo, J. Wang, J. Chen, P. Liao, J.P. Attfield, M. Yang, Angew. Chem., Int. Ed., 59 (2020) 18036-18041.

[31] Q. Lu, X. Zou, K. Liao, R. Ran, W. Zhou, M. Ni, Z. Shao, Carbon Energy, 2 (2020) 461–471.

[32] X. Liu, L. Wang, P. Yu, C. Tian, F. Sun, J. Ma, W. Li, H. Fu, Angew. Chem., Int. Ed., 57 (2018) 16166-16170.

[33] A. Saad, H. Shen, Z. Cheng, R. Arbi, B. Guo, L.S. Hui, K. Liang, S. Liu, J.P. Attfield, A. Turak, J. Wang, M. Yang, Nano-Micro Lett., 12 (2020) 79.

[34] C. Lai, M. Gong, Y. Zhou, J. Fang, L. Huang, Z. Deng, X. Liu, T. Zhao, R. Lin, K. Wang, K. Jiang, H. Xin, D. Wang, Appl. Catal., B: Environ., 274 (2020) 119086.

[35] X. Han, X. Wu, C. Zhong, Y. Deng, N. Zhao, W. Hu, Nano Energy, 31 (2017) 541-550.

[36] F. Meng, H. Zhong, D. Bao, J. Yan, X. Zhang, J. Am. Chem. Soc., 138 (2016) 10226-10231.

[37] K. He, J. Zai, X. Liu, Y. Zhu, A. Iqbal, T. Tadesse Tsega, Y. Zhang, N. Ali, X. Qian, Appl. Catal., B: Environ., 265 (2020) 118594.

[38] Z. Guo, F. Wang, Y. Xia, J. Li, A.G. Tamirat, Y. Liu, L. Wang, Y. Wang, Y. Xia, J. Mater. Chem. A, 6 (2018) 1443-1453.

[39] X.T. Wang, T. Ouyang, L. Wang, J.H. Zhong, T. Ma, Z.Q. Liu, Angew. Chem., Int. Ed., 58 (2019) 13291-13296.

[40] B.Q. Li, S.Y. Zhang, C. Tang, X. Cui, Q. Zhang, Small, 13 (2017) 1700610.

[41] W. Ni, A. Krammer, C.-S. Hsu, H.M. Chen, A. Schuler, X. Hu, Angew. Chem., Int. Ed., 58 (2019) 7445-7449.

[42] C. Zhu, A.-L. Wang, W. Xiao, D. Chao, X. Zhang, T. Nguyen Huy, S. Chen, J. Kang, X. Wang, J. Ding, J. Wang, H. Zhang, H.J. Fan, Adv. Mater., 30 (2018) 1705516.

[43] X. Wang, Q. Li, P. Shi, J. Fan, Y. Min, Q. Xu, Small, 15 (2019) 1901530.

[44] D. Gao, J. Zhang, T. Wang, W. Xiao, K. Tao, D. Xue, J. Ding, J. Mater. Chem. A, 4 (2016) 17363-17369.

[45] Y. Dong, J. Yang, Y. Liu, Y. Wang, Z. Dong, M. Cui, M. Li, X. Yuan, X. Zhang, X. Dai, Dalton Trans., 49 (2020) 6355-6362.

[46] X. Guo, X. Zheng, X. Hu, Q. Zhao, L. Li, P. Yu, C. Jing, Y. Zhang, G. Huang, B. Jiang, C. Xu, F. Pan, Nano Energy, 84 (2021) 105932.

[47] Q. Lu, J. Yu, X. Zou, K. Liao, P. Tan, W. Zhou, M. Ni, Z. Shao, Adv. Funct. Mater., 29 (2019) 1904481.

[48] M. Zhao, H.J. Peng, Z.W. Zhang, B.Q. Li, X. Chen, J. Xie, X. Chen, J.Y. Wei, Q. Zhang, J.Q. Huang, Angew. Chem., Int. Ed., 58 (2019) 3779-3783.

[49] Z. Qiu, Y. Ma, T. Edvinsson, Nano Energy, 66 (2019) 104118.

[50] W.X. Wang, S.H. Liang, T. Yu, D.H. Li, Y.B. Li, X.F. Han, J. Appl. Phys., 109 (2011) 07C501.

[51] J. Dai, Y. Zhu, Y. Yin, H.A. Tahini, D. Guan, F. Dong, Q. Lu, S.C. Smith, X. Zhang, H. Wang, W. Zhou, Z. Shao, Small, 15 (2019) 1903120.

[52] S. Nandi, S.K. Singh, D. Mullangi, R. Illathvalappil, L. George, C.P. Vinod, S. Kurungot, R. Vaidhyanathan, Adv. Energy Mater., 6 (2016) 1601189.

[53] J. Zhang, T. Wang, D. Xue, C. Guan, P. Xi, D. Gao, W. Huang, Energy Storage Mater., 25 (2020) 202-209.

[54] X.R. Wang, J.Y. Liu, Z.W. Liu, W.C. Wang, J. Luo, X.P. Han, X.W. Du, S.Z. Qiao, J. Yang, Adv. Mater., 30 (2018) 1800005.

Figures and captions
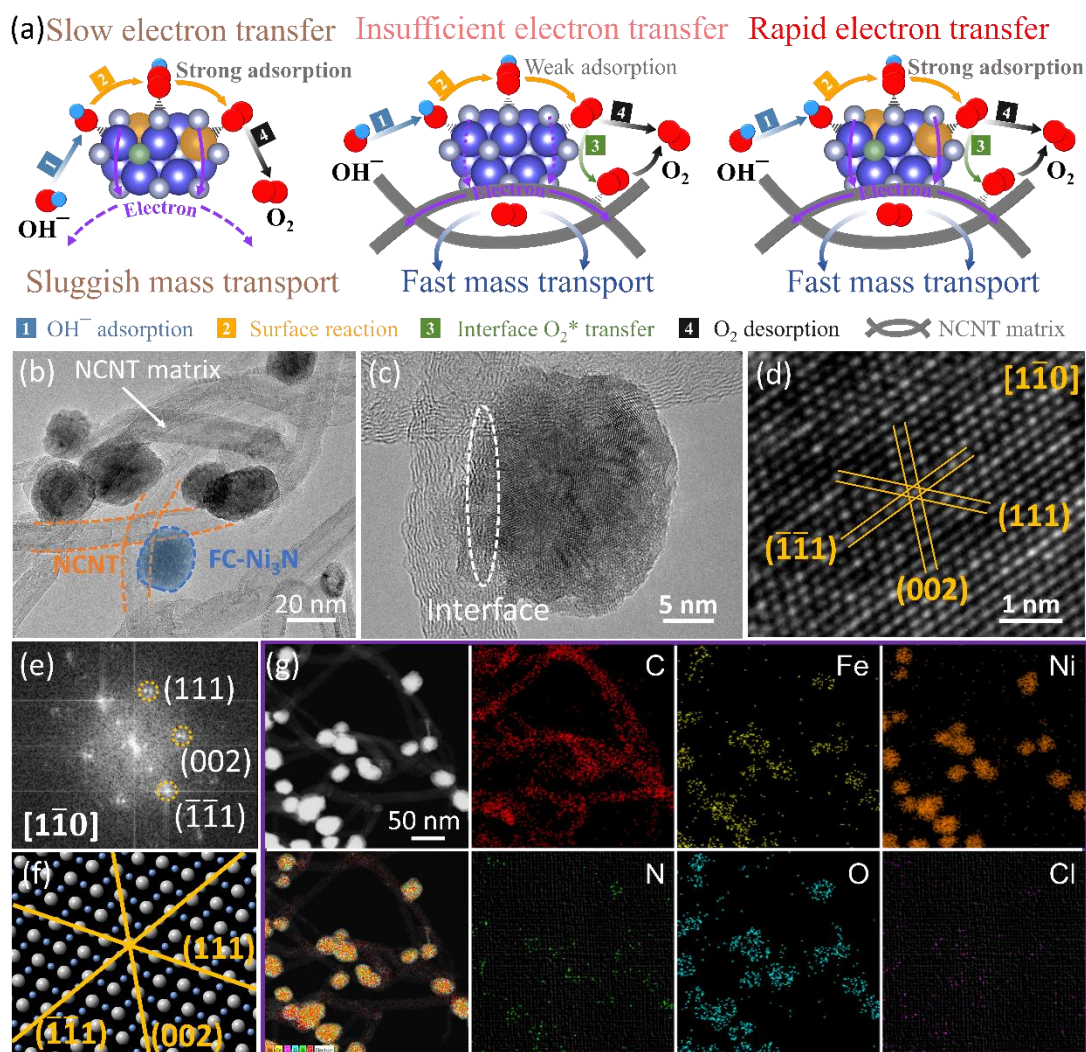
Figure 1. (a) Schematic of electron and mass transport during the OER process on different electrocatalysts (Left: FC-Ni$_3$N, Middle: Ni$_3$N/NCNT, Right: FC-Ni$_3$N/NCNT). (b) TEM and (c, d) HRTEM images of FC-Ni$_3$N/NCNT; Corresponding (e) FFT image and (f) atomic structure of the observed crystal plane; and (g) High-angle annular dark field scanning TEM (HAADF-STEM) image and corresponding elemental mapping of C, Fe, Ni, N, O, and Cl elements of FC-Ni$_3$N/NCNT.
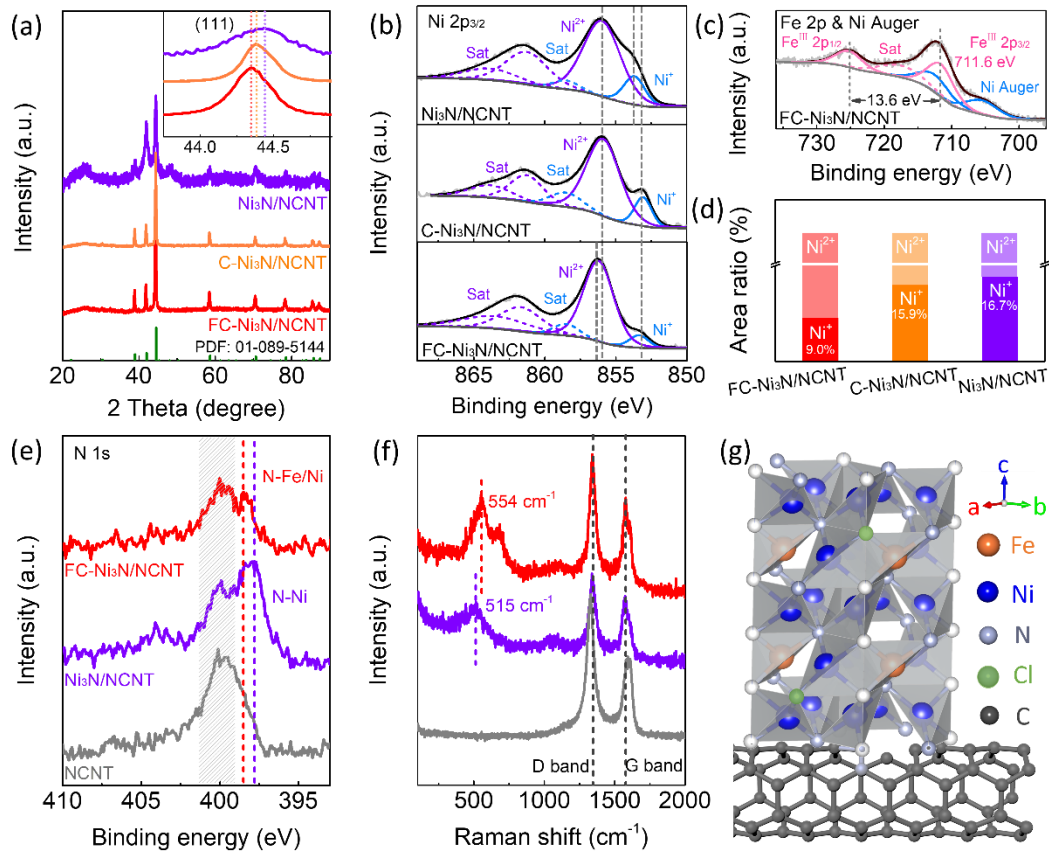
Figure 2. (a) Powder X-ray diffraction (XRD) patterns and (b) High-resolution XPS Ni 2p$_{3/2}$ spectra of the prepared samples (upper: Ni$_3$N/NCNT, middle: C-Ni$_3$N/NCNT, lower: FC-Ni$_3$N/NCNT); (c) High-resolution XPS spectra of Fe 2p and Ni auger for FC-Ni$_3$N/NCNT; (d) the comparison of the area ratio of Ni$^+$ and Ni^{2+}; (e) XPS N 1s spectra and (f) Raman scattering spectra of FC-Ni$_3$N/NCNT, Ni$_3$N/NCNT, and NCNT; (f) Schematic diagram of crystal structure for the FC-Ni$_3$N/NCNT.
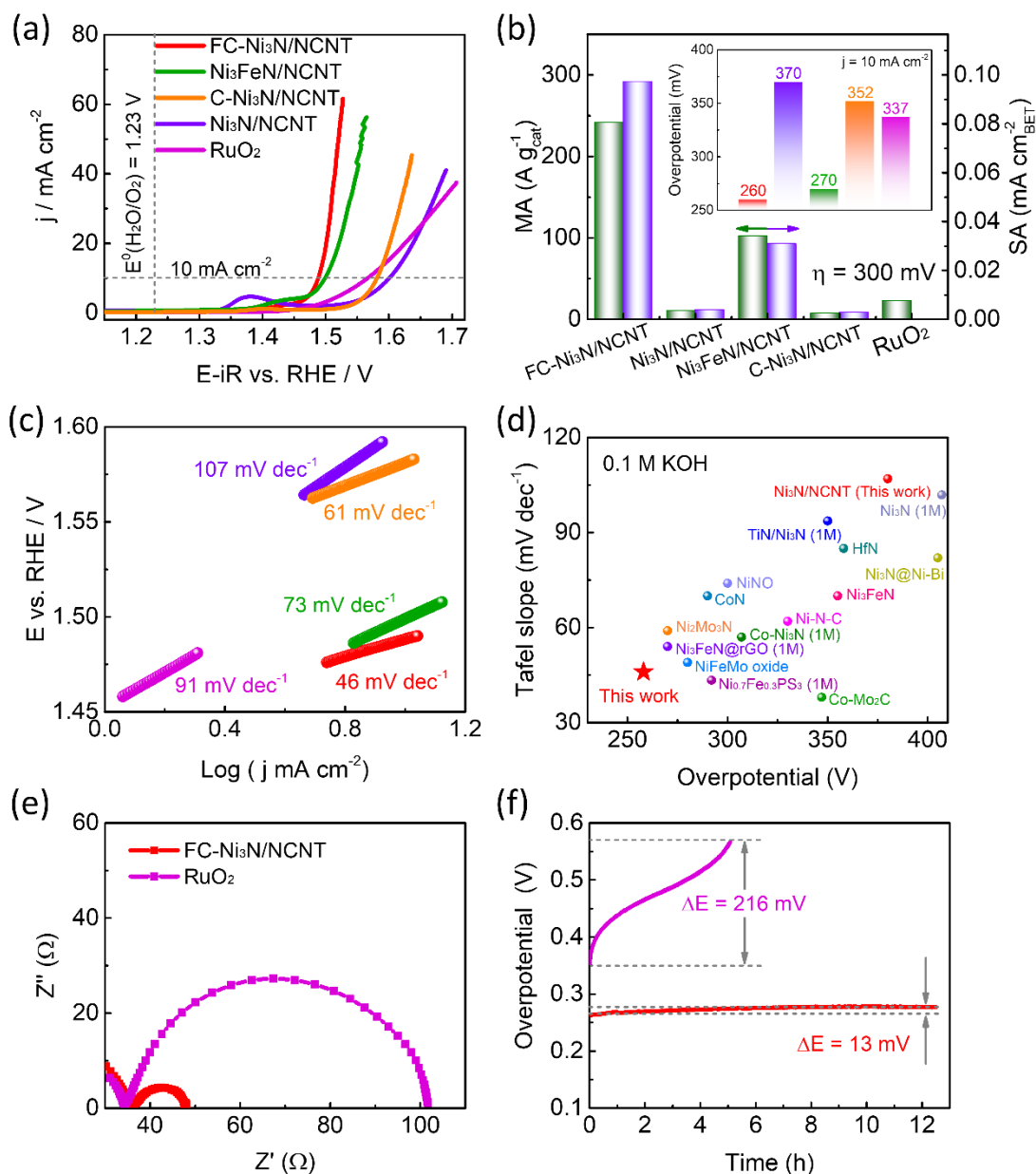
Figure 3. (a) Oxygen evolution reaction (OER) polarization curves of FC-Ni$_3$N/NCNT, Ni$_3$FeN/NCNT, C-Ni$_3$N/NCNT, Ni$_3$N/NCNT, and commercial RuO$_2$ benchmark at a scan rate of 5 mV s^{-1}; (b) Comparison of mass activity and specific activity of the selected catalysts at the overpotential of 300 mV; (c) The corresponding Tafel plots of OER for the selected catalysts; (d) Comparison of overpotentials and Tafel slopes of previous reported catalysts with this work; (e) Nyquist plots of FC-Ni$_3$N/NCNT and commercial RuO$_2$; (f) OER durability at 10 mA cm^{-2} for FC-Ni$_3$N/NCNT and commercial RuO$_2$.

25
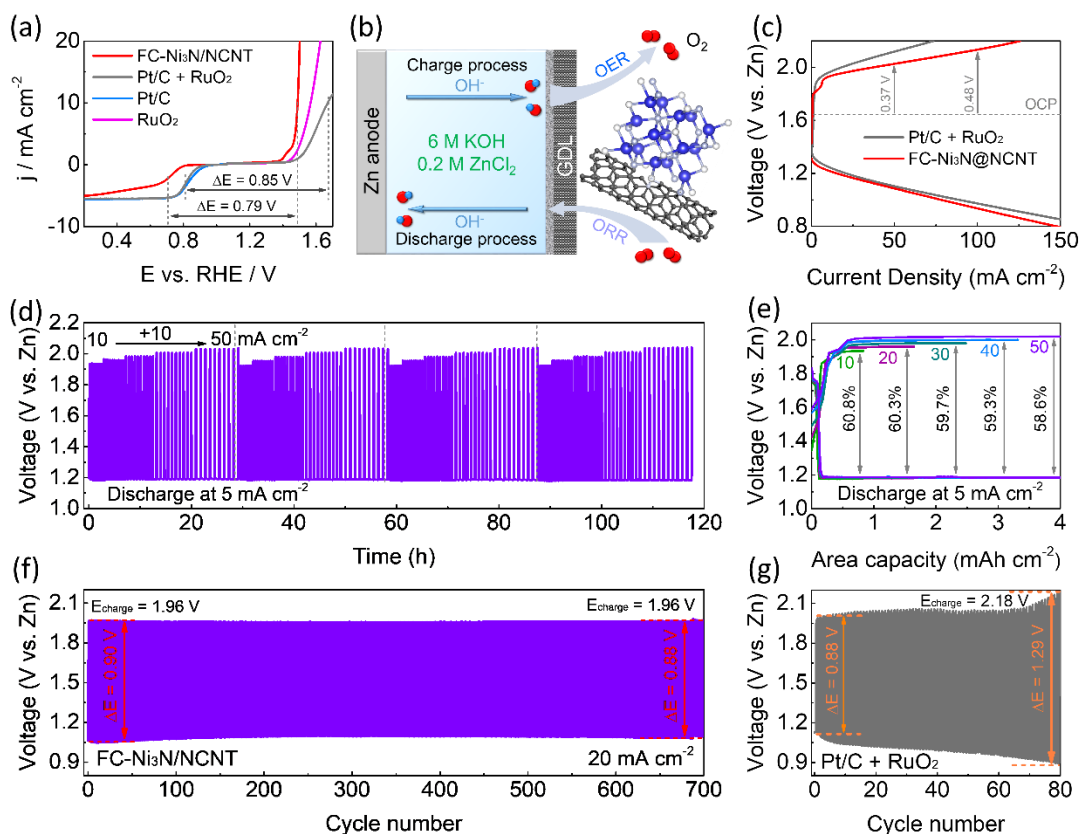
Figure 4. (a) The overall LSV curves of FC-Ni$_3$N/NCNT, Pt/C for ORR and RuO$_2$ for OER, and the mixture of Pt/C and RuO$_2$ (Pt/C + RuO$_2$); (b) Schematically depicts the structure of assembled rechargeable Zn-air battery; (c) Discharge/charge polarization curves of Zn-air batteries using FC-Ni$_3$N/NCNT and Pt/C+RuO$_2$ as catalysts at different current densities; (d) Galvanostatic charge test at different current densities (10~50 mA cm^{-2}) for FC-Ni$_3$N/NCNT; (e) Comparison of round-trip efficiency in terms of the voltage-area capacity curves of FC-Ni$_3$N/NCNT at different charging current densities; Galvanostatic charge/discharge curves of Zn-air batteries with (f) FC-Ni$_3$N/NCNT and g) Pt/C+RuO$_2$ catalysts at 20 mA cm^{-2} .
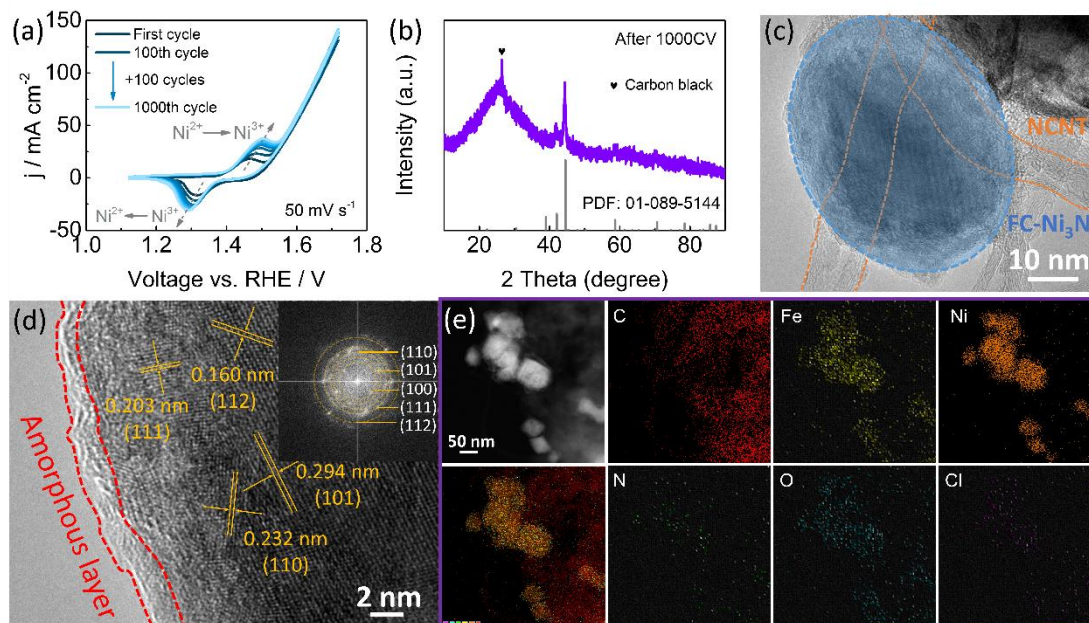
Figure 5. (a) The CV curves of FC-Ni$_3$N/NCNT over 1000 repeated cycles; (b) X-ray diffraction pattern, (c) TEM image, (d) HRTEM (insert shows the FFT pattern), and (e) HAADF-STEM image and corresponding elemental mapping of FC-Ni$_3$N/NCNT after 1000 CV test.
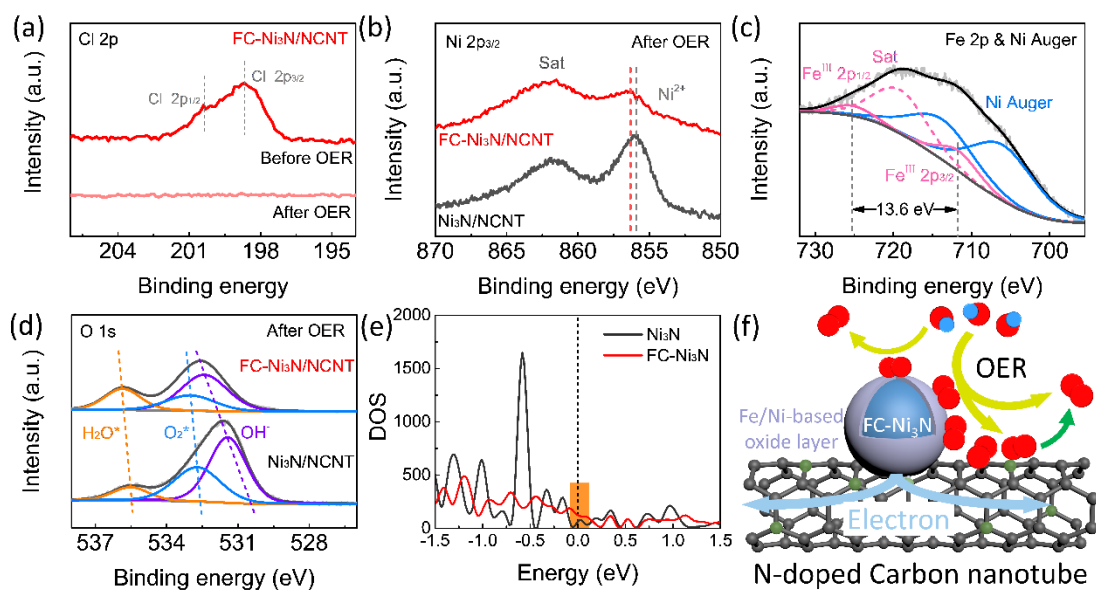
Figure 6. XPS spectra of (a) Cl 2p for FC-Ni₃N/NCNT before and after CV test, (b) Ni 2p$_{3/2}$ for FC-Ni₃N/NCNT and Ni₃N/NCNT after CV test, (c) Fe 2p for FC-Ni₃N/NCNT after CV test, (d) O 1s for FC-Ni₃N/NCNT and Ni₃N/NCNT after CV test; (e) Density of states for FC-Ni₃N/NCNT and Ni₃N/NCNT by DFT calculation. The Fermi level is set at 0 eV; (f) Mechanism of OER for FC-Ni₃N/NCNT catalyst.